Ionics (2019) 25:5229–5237
https://doi.org/10.1007/s11581-019-03076-4

ORIGINAL PAPER

In situ synthesis of porous $LiNi_{0.5}Co_{0.2}Mn_{0.3}O_2$ tubular-fiber as high-performance cathode materials for Li-ion batteries

Linsen Zhang[1] · Zhenjiang Zhao[1] · Yang Cao[1] · Lizhen Wang[1] · Hua Fang[1] · Kezheng Gao[1] · Aiqin Zhang[1] · Haili Gao[1] · Yanhua Song[1]

Received: 21 March 2019 / Revised: 15 May 2019 / Accepted: 18 May 2019 / Published online: 8 June 2019

Abstract

Hollow structural materials exhibit strong advantages for application in electrode materials. Herein, we report an in situ synthesis of hollow tubular-fiber $LiNi_{0.5}Co_{0.2}Mn_{0.3}O_2$ (HFNCM523) prepared via electrospinning combined with calcination. The features of this material were provided with fiber-interconnected 3D network structure, hollow tubular structure, and multi-scale particle gaps, which are evenly distributed on the fiber's surface. The multiple synergistic effects of these advantages result in the remarkably excellent electrochemical performance of the tubular-fiber structures with a high specific capability of 191.2 mAh g^{-1} at 0.1 C and 84% high rate capacity retention after 100 cycles at 1 C. In particular, the $LiNi_{0.5}Co_{0.2}Mn_{0.3}O_2$ hollow tubular-fiber structure was well maintained after 100 cycles.

Keywords Tubular fiber · $LiNi_{0.5}Co_{0.2}Mn_{0.3}O_2$ · Electrospinning · Electrochemical performance

Introduction

Layer-structured ternary materials $LiNi_xCo_yMn_{1-x-y}O_2$ had attracted attention as a cathode material due to its stable structure, compositional flexibility, and high reversible capacities [1–4]. Among these materials, $LiNi_{0.5}Co_{0.2}Mn_{0.3}O_2$ (NCM523) is viewed as a promising candidate due to its relatively high energy density and low cost [5, 6].

The preparation of the precursor is involved in the traditional synthesis of layer-structured ternary materials $LiNi_xCo_yMn_{1-x-y}O_2$. The precursor plays an important role in its electrochemical performance. The geometry, size, tap density, and homogeneity of precursors largely determine the performance of the final products [7, 8]. Therefore, many approaches were adopted to synthesize NCM523 precursors, such as hydrothermal method [9], hydroxide co-precipitation [10], carbonate co-precipitation [11], and sol–gel method [12]. However, such preparation methods are complicated and time-consuming. These conventional synthetic methods also typically involve subsequent mixing of lithium with the precursor and calcination at elevated temperatures to obtain the final products, which greatly increase production cost. Based on such considerations, the exploitation of high-efficiency and cost-effective preparation strategies is of great importance for energy storage technology.

Fortunately, in recent years, the electrospinning technique is widely used in many fields as an effective and inexpensive way of truly producing 1D fibers structure from micrometer to nanometer size ranges in diameter, including the fabrication of electrode materials, especially anode and cathode materials for Li-ion batteries [13–17]. The process of subsequent lithium mixing is reduced compared with the traditional preparation strategy. Instead, the transition metal and lithium salts are added together during the preparation of the 1D precursor, which could be synthesized in situ to acquire the desired products. In addition, 1D nanostructures including nanowires [18], nanobelts [19], nanofibers [20], nanorods [21], and nanotubes [22, 23], also show great advantages due to their unique physicochemical properties as follows: (1) 1D materials provide a direct path for electron transport, which is more conducive to electron transfer than nanoparticles. (2) They exhibit fast ion transport. The ion diffusion time constant in the electrode material is proportional to the square of the diffusion path. Wherein the shorter the diffusion path, the smaller the time

✉ Linsen Zhang
hnzhanglinsen@163.com

[1] Henan Provincial Key Laboratory of Surface and Interface Science, School of Material and Chemical Engineering, Zhengzhou University of Light Industry, Zhengzhou 450002, China

constant and the higher the electrode magnification performance. (3) The specific surface area of the 1D material is large, which ensures the contact area between the electrode and the electrolyte and the electrochemical active site. (4) The 1D material can adapt to the volume expansion of the electrode material and inhibit mechanical degradation, thereby ensuring the long cycle life of the electrode.

Therefore, in situ synthesis of electrospinning technology was utilized in this work to produce NCM523. The effect of temperature on the structure and the electrochemical properties of NCM523 were investigated in detail. As expected, the obtained materials with exquisite 1D hollow fiber structure exhibited superior cyclic capability, which results from the novel structure that provides fast transport channels for electrons and lithium ions as well as the hollow architecture that helped to alleviate the structure changes caused by the lithium insertion/extraction during cycling.

Experimental

Preparation of $LiNi_{0.5}Co_{0.2}Mn_{0.3}O_2$ hollow fibers

The 1D hollow tubular-fiber $LiNi_{0.5}Co_{0.2}Mn_{0.3}O_2$ was synthesized via electrospinning and subsequent heat treatment. Typically, the first step for the preparation is dissolving the stoichiometric amount of Ni $(CH_3COO)_2{\cdot}4H_2O$, Co $(CH_3COO)_2{\cdot}4H_2O$, Mn $(CH_3COO)_2{\cdot}4H_2O$, and $LiCH_3COO{\cdot}4H_2O$ in 20 g absolute ethanol. Therefore, the mixture was stirred vigorously at room temperature for 12 h to form a homogeneous transparent solution. Afterwards, 1.5 g of PVP (M_w = 1,300,000) was added in the above solution and the mixed solution was further stirred at room temperature for 12 h to form an electrospinning solution. The resultant spinning solution was then transferred to a plastic syringe with a 19 G stainless steel needle (inner diameter 0.92 mm). Electrospinning was carried out with a flow rate of 0.5 mL h^{-1}, a needle-to-collector distance of 120 mm, a humidity of 25%, a temperature of 25 °C, and a voltage of 25 kV. A high-voltage generator was used to provide a high voltage for electrospinning. Fibers were collected and placed on an aluminum foil as a mat. The schematic illustration for the synthesis of $LiNi_{0.5}Co_{0.2}Mn_{0.3}O_2$ hollow fibers is shown in Fig. 1. First, the intertwined fibers with a smooth surface were obtained via electrospinning. The as-spun fibers were calcinated at 700 °C, 725 °C, 750 °C, 775 °C, and 800 °C for 20 h in the air to obtain the hollow tubular products, denoted as HF700, HF725, HF750, HF775, and HF800, respectively.

Physical characterization

Powder x-ray diffraction (XRD, D8-ADVANCE) of the as-prepared materials equipped with Cu-Kα (λ = 1.5418 Å) radiation was performed to investigated the structure of the samples. Field emission scanning electron microscopy (FESEM, JEOL-JSM-7100F) equipped with energy-dispersive x-ray spectroscopy (EDS) and high-resolution electron microscopy (HRTEM, JEOL JEM-2100, Japan) were employed to investigate the morphologies and elemental distributions of the products. Results of the thermogravimetry analysis (TGA) of the sample were recorded with a Netzsch STA 449-F3 thermogravimetric analyzer at a heating rate of 5 °C/min in air.

Electrochemical characterization

Electrochemical performance measurements were conducted using a CR2016 cell. Working electrodes were prepared by mixing 85 wt% as-prepared materials, 10 wt% Super P, and 5 wt% polyvinylidene fluorides, dissolved in N-methylpyrrolidinone and formed uniform slurry. The slurry was spread on an aluminum foil and dried. Cells were assembled in an Ar-filled glove box with Li foil as counter electrode, Celgard 2400 as separator, and 1 mol L^{-1} $LiPF_6$ in a 1:1 (by volume) mixture of ethylene carbonate and ethyl methyl carbonate as electrolyte. The galvanostatic charge/discharge tests were performed between 2.7 and 4.5 V (1 C = 200 mA g^{-1}) using a NEWARE battery tester. Cyclic voltammetry (CV, 2.7–4.5 V, 0.1 mV s^{-1}) and electrochemical impedance spectroscopy (EIS, 10^5–10^{-2} Hz) were conducted using an electrochemical workstation (CHI660E). All tests were conducted at room temperature.

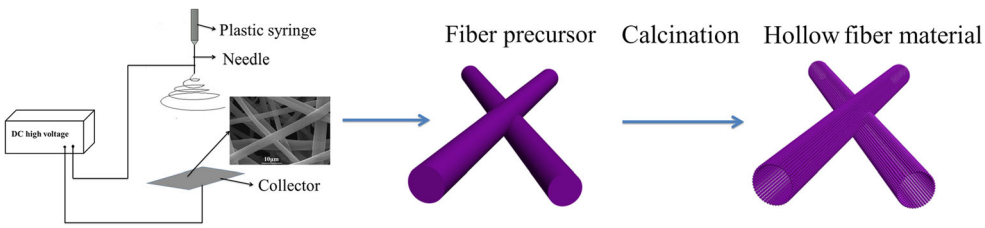

Fig. 1 Schematic illustration of the synthesis procedure for $LiNi_{0.5}Co_{0.2}Mn_{0.3}O_2$ hollow fibers

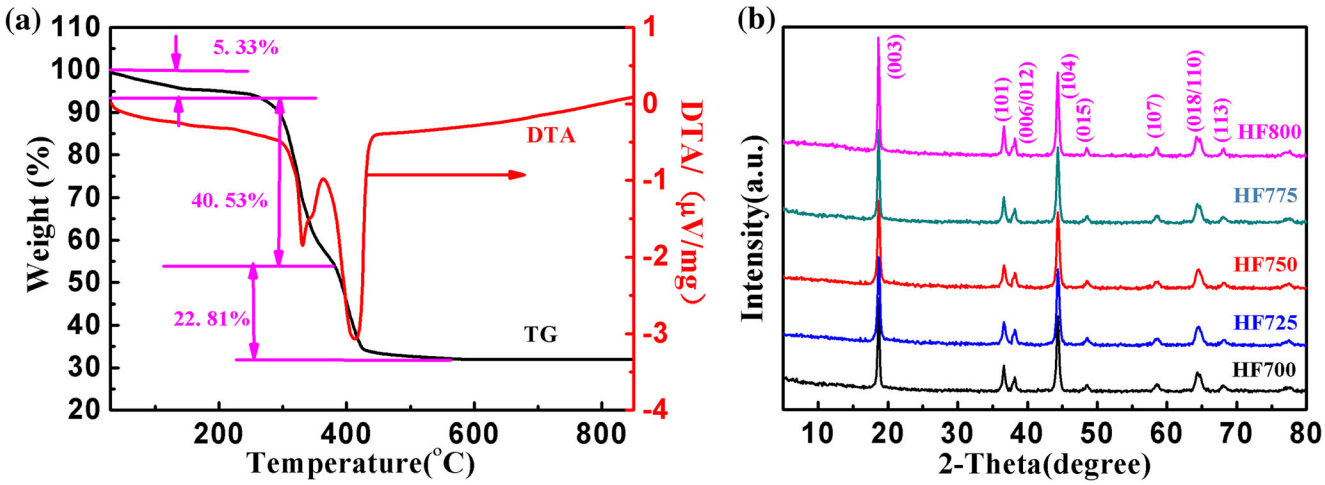

Fig. 2 **a** TG-DTA curves of the fiber precursor. **b** XRD patterns of fiber cathode material at different temperatures

Results and discussion

Physical characterization

TG-DTA was performed in air to investigate the thermal decomposition behavior of fibers in Fig. 2a. Results in Fig. 2a indicate that the fibers have three distinct weight loss steps with a total weight loss of 68.67 wt%. The first lost stage was approximately 5.33 wt% weight below 260 °C, which is due to the removal of the absorbed moisture and ethanol from the metal salt precursors. The largest weight loss of around 40.53 wt% occurred between 280 and 380 °C owing to the decomposition of metal salts as shown by the DTA curve, indicating an obvious endothermic peak within this temperature range. Finally, 22.81 wt% mass thermal decomposition loss is associated with polymers occurred at around 410 °C with an obvious endothermic peak at about 410 °C. Above 600 °C, no obvious quality loss was observed, indicating the complete decomposition of the polymers.

Figure 2b shows the XRD patterns of the as-prepared $LiNi_{0.5}Co_{0.2}Mn_{0.3}O_2$ fibers calcined at different temperatures. All the samples exhibited almost identical diffraction peaks, which can be indexed to a well-fine hexagonal layered α-$NaFeO_2$ structure with R-3m space group [24]. The obvious splitting diffractive peaks at (006)/(012) and (018)/(110) indicate the highly ordered layered structure. However, the splitting peaks of 006/012 and 018/110 is not obvious when the sample obtained at low temperature such as HF700, which could be attributed to the low sintering temperature will result in insufficient crystallization of the layered structure. Referring to the literature [25], the lithiation process is a phase transformation process in which lithium and oxygen are inserted into the crystal surface causing surface reconstruction at low temperature. The surface reconstruction caused an extensive migration of Ni atoms to the surface and result in a strong Ni segregation on the crystal surface, so that the heterostructured phase was formed during the low temperature. Low sintering temperature will result in insufficient crystallization of the layered structure. So, the splitting peaks of 006/012 and 018/110 indicating layered structure degree is not obvious when the sample obtained at low temperature. The lattice parameters of the resultant samples were obtained and summarized in Table 1. The ratio of *c*/*a* is an important parameter to the layer structure [26]. Generally, a high value of *c*/*a* indicates a good layer structure. The largest *c*/*a* value of HF750 implies that it has a highly ordered layered structure, which is beneficial for electrochemical performance.

Table 1 Lattice parameters and integrated intensity rations of all samples

Samples	*a*/(Å)	*c*/(Å)	*c*/*a*
HF700	2.8729	14.1466	4.9242
HF725	2.8638	14.1478	4.9402
HF750	2.8756	14.2597	4.9588
HF775	2.8812	14.2822	4.9570
HF800	2.8762	14.2222	4.9448

Figure 3 shows the morphologies of the synthesized fiber precursors and the final products at series temperatures. The as-electrospun fiber precursors in Fig. 3a and b with a smooth surface have a disordered interlaced arrangement with the diameter that is uniformly distributed in the range of 1.5–2 μm. The 1D structure was maintained after calcination at different temperature. Meanwhile, the as-obtained samples displayed similar hollow fiber structure. The fiber morphology of the samples is also relatively regular when the calcination temperature is below 775 °C, as shown in Fig. 3c–h. Among them, HF750 (Fig. 3g, h) exhibits the most regular tubular structure and has numerous pores distributed on the tube wall. Figure 3i and j presents an image of HF775, depicting a change for the hollow tubular structure, and the particle sizes of the fibers become larger. Figure 3k and l shows that the tubular structure of the HF800 samples begins to flatten, and the pores on the

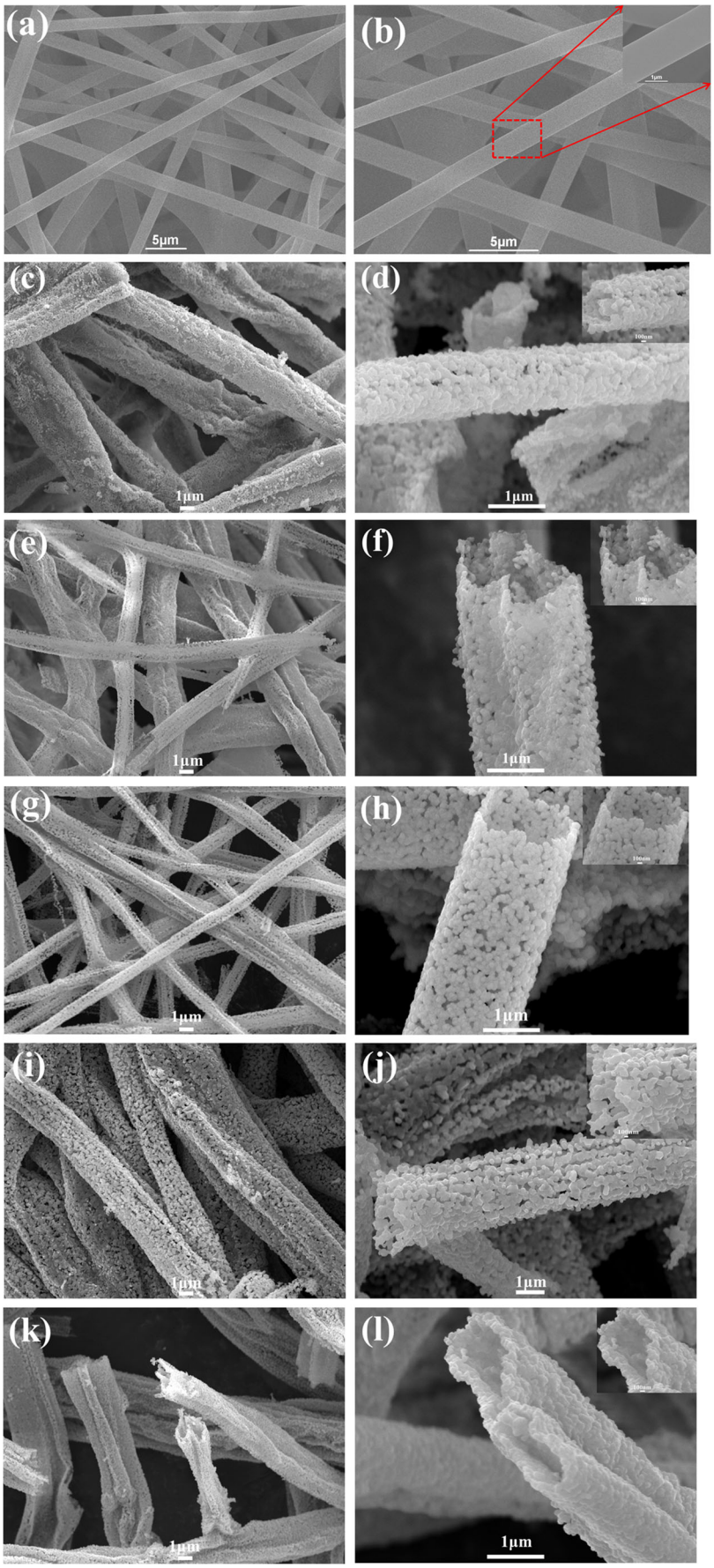

Fig. 3 SEM images of the samples. **a**, **b** fiber precursor. **c**, **d** HF700. **e**, **f** HF725. **g**, **h** HF750. **i**, **j** HF775. **k**, **l** HF800

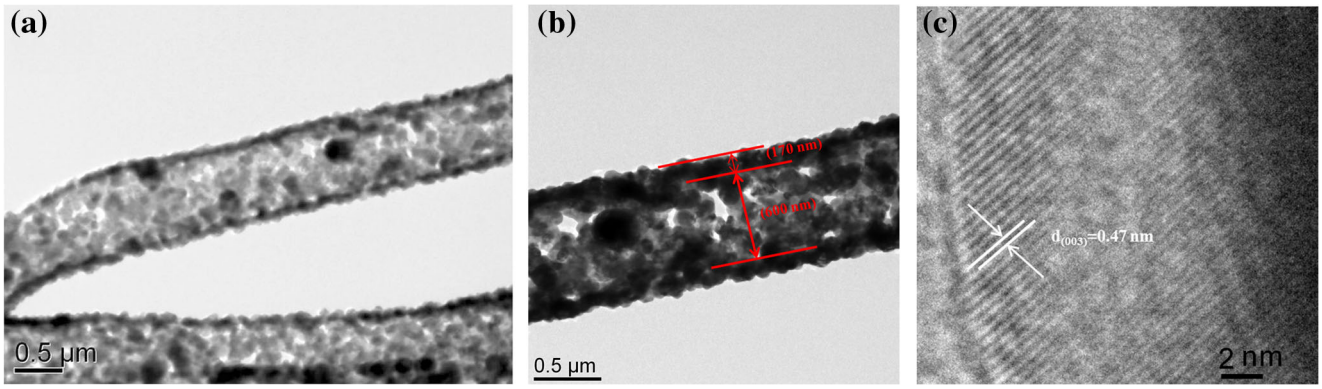

Fig. 4 **a**, **b** TEM images of HF750 and **c** HRTEM image of HF750

fiber wall disappeared, which can be attributed to a very high calcination temperature.

The TEM images of HF750 are shown in Fig. 4. The strong contrast between the dark edges and the bright inside space indicates that the samples are hollow in Fig. 4a. Figure 4b further confirmed the well-defined tubular structure with the thickness about 170 nm of tube wall and 600 nm of the tube inner diameter. The rough and porous surfaces of the hollow tube are composed of many small NCM523 nanoparticles. The HRTEM image (Fig. 4c) confirms the high crystallinity of the hollow tubular fiber. Results of the XRD analysis indicate that the lattice fringe has a spacing of ca. 0.47 nm which corresponds to a (003) plane of layered structure of the NCM523.

Figure 5a presents the initial charge/discharge curves of all samples at 0.1 C. HF750 delivered a higher initial discharge

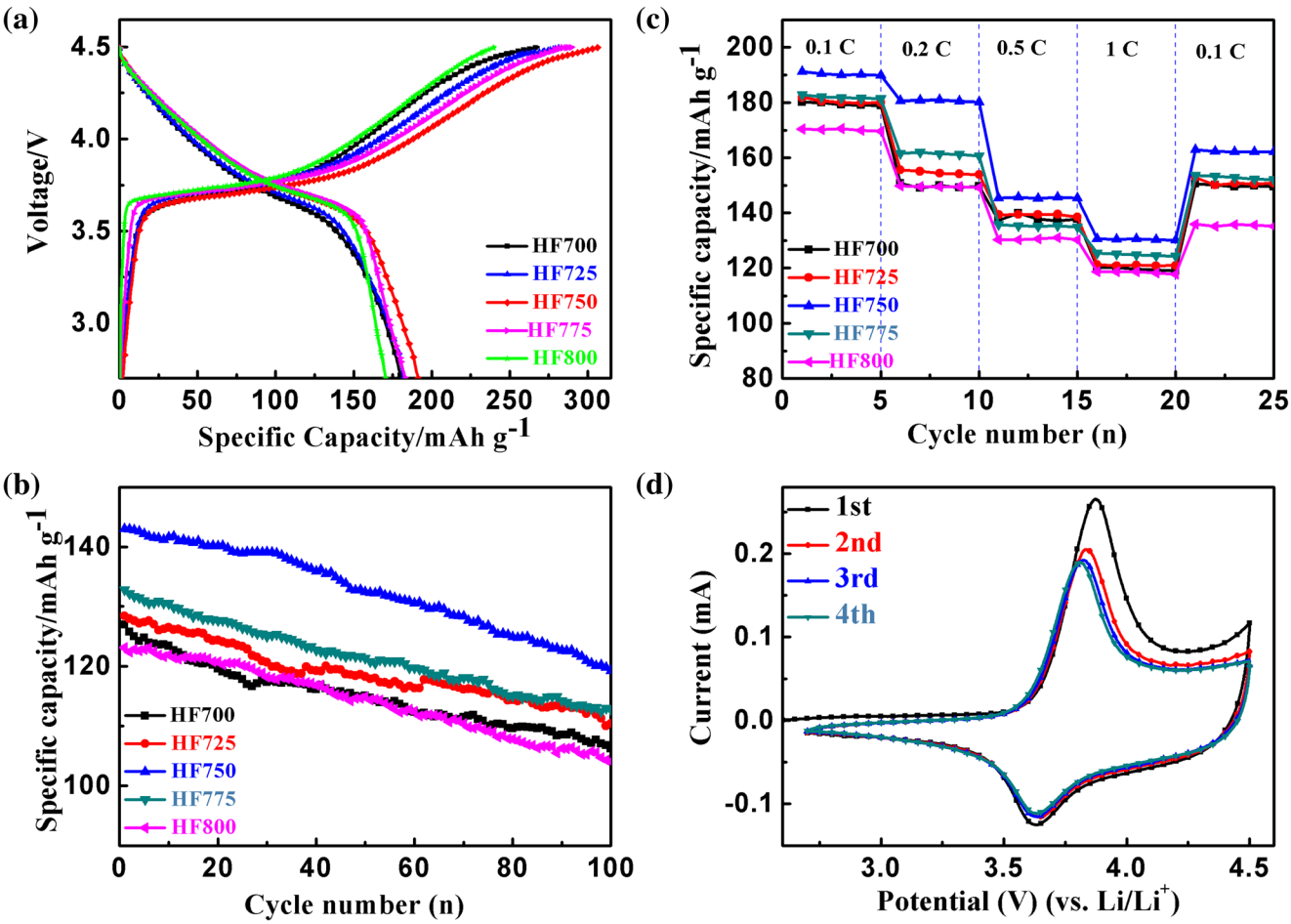

Fig. 5 **a** Initial charge/discharge curves of samples at 0.1 C. **b** Cycling performance at 1 C. **c** Rate capability of samples. **d** CV curves of the HF750 electrode

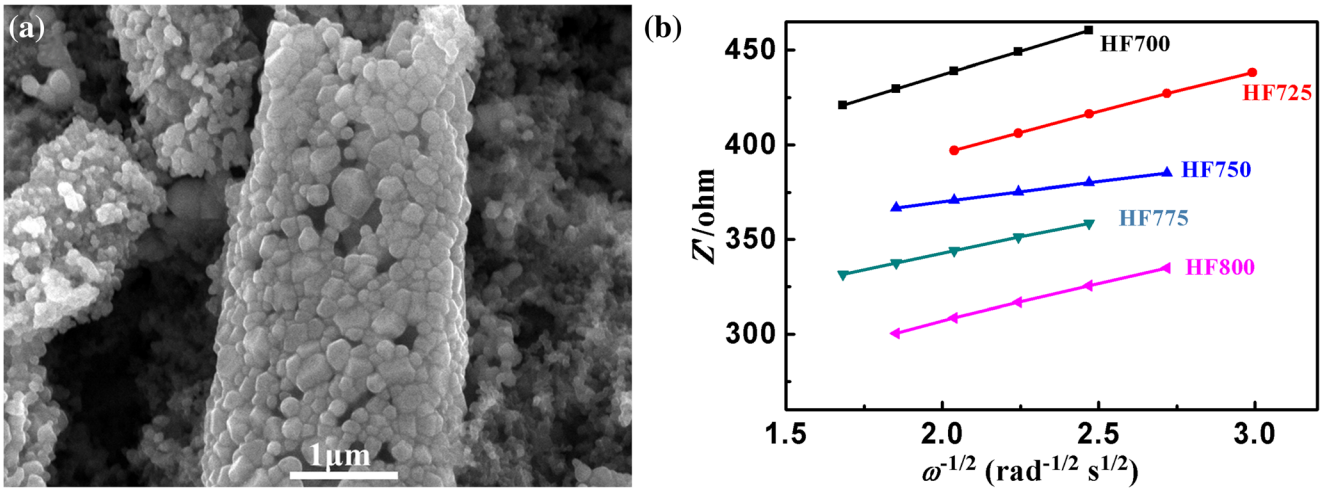

Fig. 6 **a** Nyquist plots of electrodes after three cycles charged to 4.0 V with the corresponding equivalent circuit model (inset). **b** the $Z' - \omega^{-1/2}$ curves after three cycles charged to 4.0 V

capacity of 191.2 mAh g^{-1}, whereas others had a lower initial capacity. The HF800 sample exhibited the lowest discharge capacity, which may be attributed to a certain degree of damage to the hollow structure at excessively high temperatures. These results show that the calcination temperature is crucial to electrochemical performance. Figure 5b depicts the cycling performance of samples at 1 C, showing that the HF750 electrode material exhibited a superior cyclic stability. After 100 cycles, 84% of the capacity retention can be obtained, indicating that the HF750 electrode has a remarkable stability. Figure 5c shows the rate properties of the samples at variable rates from 0.1 to 1 C. Obviously, the HF750 electrode displayed a relatively higher reversible capacity than the other samples at various current rates.

The first four CV curves of HF750 are presented in Fig. 5d. All curves exhibit only one redox couple, corresponding to the Ni^{2+}/Ni^{4+} redox reaction [27–29]. The voltage difference (ΔEp) between the oxidation and reduction peaks reflects the degree of electrochemical reversibility and polarization of the as-prepared electrodes [30]. The ΔEp between the anodic peak potential and cathodic peak potential of the HF750 electrode for the first four cycles are 0.235, 0.187, 0.185, and 0.183 V, respectively. The gradually decreasing potential difference indicates a good electrochemical reversibility and low polarization of the electrode, which are good and consistent with the results of the cycle performance tests discussed above. Based on the above analysis, 750 °C is the optimal calcination temperature, and the resulting 1D structure and porous surface ensure excellent electrode–electrolyte contact, while the hollow structure provides a short pathway for electron and Li^+ diffusion, both of which could significantly improve electrochemical performance.

Figure 6a shows the Nyquist plots of all samples after three cycles. The intercept of semicircle at the high frequency region is assigned to the ohm impedance (R_s), the semicircle in the high and middle-frequency region is regarded as the sum of film resistance (R_f) and the charge transfer resistance (R_{ct}); Among, the film resistance (R_f) derived from the formation of SEI film during activation. And the straight line the in low-frequency region corresponds to the Warburg impedance (W) [31–33]. Notably, the sum of R_f and R_{ct} of HF750 is the smallest among the samples (Table 2), demonstrating its superior electrode kinetics characteristics. Accordingly, the outstanding electrochemical performance delivered by HF750 cathode material can be attributed to its relatively low polarization rate that is benefited by its sophisticated and unique hollow tubular-fiber structure, which is in good agreement with the above electrochemical tests. The sloping line of EIS in the low-frequency region is related to Li^+ diffusion in electrode, and the diffusion coefficient (D) can be further calculated using the following equation [34, 35]:

$$D = \frac{R^2T^2}{2A^2n^4F^4C^2\sigma^2},$$

where R is the gas constant, T is the absolute temperature, A is the electrode area, n is the number of electrons transferred involved in reaction, F is the Faraday constant, C is the molar concentration of Li^+ in the electrode, and σ is the Warburg

Table 2 Parameters of impedance spectra and Li^+ ion diffusion coefficients of samples after three cycles

Samples	R_s (Ω)	$R_f + R_{ct}$ (Ω)	D_{Li^+} (cm^2 s^{-1})
HF700	4.8	258.1	5.53×10^{-11}
HF725	3.7	209.7	7.34×10^{-11}
HF750	3.9	161.2	3.77×10^{-10}
HF775	3.5	168.4	1.18×10^{-10}
HF800	4.0	261.5	8.81×10^{-11}

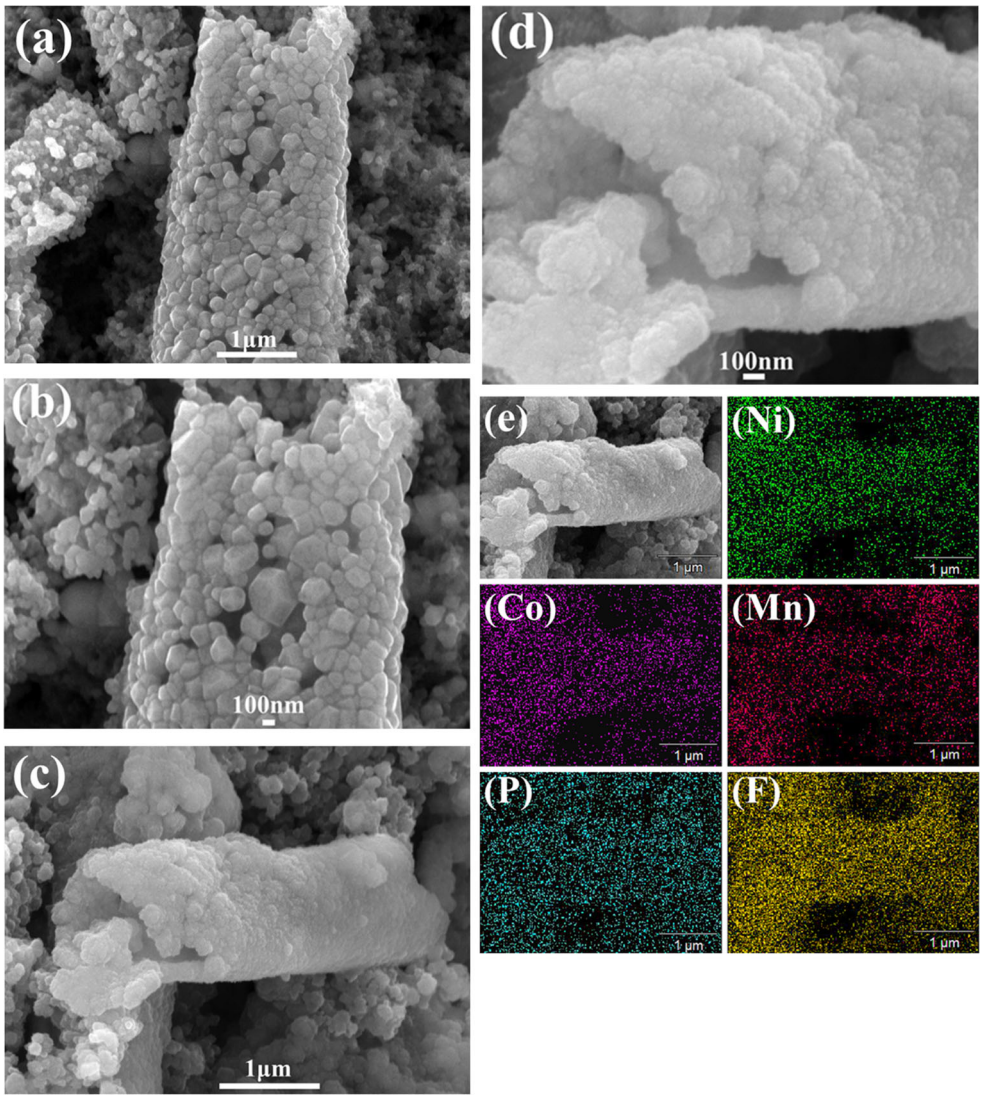

Fig. 7 **a**, **b** SEM images of HF750 electrodes before the cycle. **c**, **d** Electrodes after 100 cycles at 1 C. **e** Corresponding elemental mapping images

impedance coefficient, which can be obtained from the slope of $Z' - \omega^{-1/2}$ relationship at low frequency as shown in Fig. 6b [36]. The Li^+ diffusion coefficient of the samples after three cycles were calculated and summarized in Table 2. The higher *D* of HF750 than those of the other samples indicating that its good structure facilitates the diffusion of Li^+, which further explains its excellent electrochemical performance.

For the sake of exploring the structural properties of HF750 electrode materials, The SEM images of HF750 electrodes before and after 100 cycles at 1 C are shown in Fig. 7. In contrast to the morphologies of the electrodes before cycling (Fig. 7a, b), (Fig. 7c and d shows that the morphology of HF750 hardly changed and it remained maintaining a hollow tubular-fiber structure, indicating its good structural stability, which further proves the excellent cycle performance of HF750 (Fig. 5b). The mapping results in Fig. 7e indicate the presence and homogeneous distribution of Ni, Co, Mn, P, and F. A series of results indicates the superior structural stability of the NCM523 hollow tubular 1D cathode material.

Conclusions

This paper reported an in situ synthesis of the hollow tubular NCM523, which is reported as a new high-stability cathode material for Li-ion batteries. Calcination temperature is critical to the electrochemical properties of the hollow tubular-fiber NCM523. The as-prepared HF750 exhibited the best electrochemical performance with retention of 84% after 100 cycles at 1 C, which is attributed to the well-guided charge transfer kinetics with short ionic diffusion pathways of the hollow fiber structure, as well as the large effective contact area with the electrolyte during cycling.

Funding This work is supported by foundation of Henan Provincial Natural Science Foundation (No. 162300410315), foundation of Henan Provincial science and technology research (No. 182102210163), create space hatching project foundation of Zhengzhou University of Light Industry (No. 2017ZCKJ205), and scientific research foundation of Zhengzhou University of Light Industry in 2015 (No. 2015XJJZ036).

References

1. Xia Y, Zheng J, Wang C, Gu M (2018) Designing principle for Ni-rich cathode materials with high energy density for practical applications. Nano Energy 49:434–452
2. Kim J, Lee H, Cha H, Yoon M, Park M, Cho J (2018) Nickel-rich cathodes: prospect and reality of Ni-rich cathode for commercialization. Adv Energy Mater 8(6):1702028
3. Manthiram A, Song B, Li W (2017) A perspective on nickel-rich layered oxide cathodes for lithium-ion batteries. Energy Storage Mater 6:125–139
4. Yang H, Wu H-H, Ge M, Li L, Yuan Y, Yao Q, Chen J, Xia L, Zheng J, Chen Z, Duan J, Kisslinger K, Zeng XC, Lee W-K, Zhang Q, Lu J (2019) Simultaneously dual modification of Ni-rich layered oxide cathode for high-energy lithium-ion batteries. Adv Funct Mater 29(13):1808825
5. Yang J, Yu Z, Yang B, Liu H, Hao J, Yu T, Chen K (2018) Electrochemical characterization of Cr_8O_{21} modified $LiNi_{0.5}Co_{0.2}Mn_{0.3}O_2$ cathode material. Electrochim Acta 266: 342–347
6. Shim JH, Im J, Kang H, Cho N, Kim YM, Lee S (2018) Implications of cation-disordered grain boundary on the electrochemical performance of $LiNi_{0.5}Co_{0.2}Mn_{0.3}O_2$ cathode material for lithium ion batteries. J Mater Chem A 6:16111–16120
7. Xu L, Zhou F, Kong J, Zhou H, Zhang Q, Wang Q, Yan G (2018) Influence of precursor phase on the structure and electrochemical properties of Li $(Ni_{0.6}Mn_{0.2}Co_{0.2})O_2$ cathode materials. Solid State Ionics 324:49–58
8. Wang M, Luo M, Chen Y, Chen L, Yan S, Ren Y, Chu M (2017) A new approach to improve the electrochemical performance of Li-rich cathode material by precursor pretreatment. J Alloys Compd 696:891–899
9. Shi Y, Zhang M, Fang C, Meng YS (2018) Urea-based hydrothermal synthesis of $LiNi_{0.5}Co_{0.2}Mn_{0.3}O_2$ cathode material for Li-ion battery. J Power Sources 394:114–121
10. Zhao R, Yang Z, Liang J, Lu D, Liang C, Guan X, Gao A, Chen H (2016) Understanding the role of Na-doping on Ni-rich layered oxide $LiNi_{0.5}Co_{02}Mn_{03}O_2$. J Alloys Compd 689:318–325
11. Zhang Z, Zhu S, Huang J, Yan C (2016) Acacia gum-assisted co-precipitating synthesis of $LiNi_{0.5}Co_{0.2}Mn_{0.3}O_2$ cathode material for lithium ion batteries. Ionics 22(5):1–7
12. Kong JZ, Zhai HF, Ren C, Gao MY, Zhang X, Li H, Li JX, Tang Z, Zhou F (2013) Synthesis and electrochemical performance of macroporous $LiNi_{0.5}Co_{0.2}Mn_{0.3}O_2$ by a modified sol-gel method. J Alloys Compd 577(45):507–510
13. Liu Y, Yan X, Xu B, Lan J, Yu Y, Yang X, Lin Y, Nan C (2018) Self-reconstructed formation of a one-dimensional hierarchical porous nanostructure assembled by ultrathin TiO_2 Nanobelts for fast and stable Lithium storage. ACS Appl Mater Interfaces 10(22):19047–19058
14. Liu Y, Li L, Zhu J, Meng T, Ma L, Zhang H, Xu M, Jiang J, Li CM (2018) One-dimensional integrated MnS@carbon nanoreactors hybrid: an alternative anode for full-cell Li-ion and Na-ion batteries. ACS Appl Mater Interfaces 10(33):27911–27919
15. Kacica CT, Wang LS, Chadha TS, Biswas P (2018) Oriented, one-dimensional tin dioxide-titanium dioxide composites as anode materials for lithium-ion batteries. Energy Technol 6:1966–1974
16. Ma D, Li Y, Zhang P, Cooper AJ, Abdelkader AM, Ren X, Deng L (2016) Mesoporous $Li_{1.2}Mn_{0.54}Ni_{0.13}Co_{0.13}O_2$ nanotubes for high-performance cathodes in Li-ion batteries. J Power Sources 311:35–41
17. Liu Q, Zhu J, Zhang L, Qiu Y (2018) Recent advances in energy materials by electrospinning. Renew Sust Energ Rev 81:1825–1858
18. Qiu Y, Fan H, Chang X, Dang H, Luo Q, Cheng Z (2018) Novel ultrathin Bi_2O_3 nanowires for supercapacitor electrode materials with high performance. Appl Surf Sci 434:16–20
19. Lv C, Peng Y, Yang J, Duan X, Ma J, Wang T (2018) Electrospun Nb-doped $LiNi_{0.4}Co_{0.2}Mn_{0.4}O_2$ nanobelts for lithium-ion battery. Inorg Chem Front 5:1126–1132
20. Ji X, Li D, Lu Q, Guo E, Yao L, Liu H (2017) Electrospinning preparation of one-dimensional Co^{2+}-doped $Li_4Ti_5O_{12}$ nanofibers for high-performance lithium ion battery. Ionics 19(12):1–8
21. Han Z, Wang B, Liu X, Wang G, Wang H, Bai J (2018) Peapod-like one-dimensional (1D) CoP hollow nanorods embedded into graphene networks as an anode material for lithium-ion batteries. J Mater Sci 53(11):1–15
22. Yang W, Chen Y, Wang J, Peng T, Xu J, Yang B, Tang K (2018) Reduced graphene oxide/carbon nanotube composites as electrochemical energy storage electrode applications. Nanoscale Res Lett 13(1):181–187
23. Leng J, Wang Z, Li X, Guo H, Yan G, Hu Q, Peng W, Wang J (2019) A novel dried plum-like yolk-shell architecture of tin oxide nanodots embedded into a carbon matrix: ultra-fast assembly and superior lithium storage properties. J Mater Chem A 7(10):5803–5810
24. Mo Y, Hou B, Li D, Jia X, Cao B, Yin L, Chen Y (2016) Enhanced high-rate capability and high voltage cycleability of Li_2TiO_3-coated $LiNi_{0.5}Co_{0.2}Mn_{0.3}O_2$ cathode materials. RSC Adv 6:88713–88718
25. Hua W, Chen M, Schwarz B, Knapp M, Bruns M, Barthel J, Yang X, Sigel F, Azmi R, Senyshyn A, Missiul A, Simonelli L, Etter M, Wang S, Mu X, Fiedler A, Binder JR, Guo X, Chou S, Zhong B, Indris S, Ehrenberg H (2019) Lithium/oxygen incorporation and microstructural evolution during synthesis of Li-rich layered Li $[Li_{0.2}Ni_{0.2}Mn_{0.6}]O_2$ Oxides. Adv Energy Mater 9(8):1803094
26. Jiang Q, Gao Y, Peng J, Li H, Liu Q, Jiang L, Lu X, Hu A (2018) Effects of polyvinyl alcohol on the electrochemical performance of $LiNi_{0.8}Co_{0.15}Al_{0.05}O_2$ cathode material. J Solid State Electrochem 22:1–7
27. Ren T, Zhang J, Wang D, Dong P, Duan J, Li X, Rao S, Huang D, Zhang Y (2018) Enhancing the high-voltage performances of Ni-rich cathode materials by homogeneous La_2O_3 coating via a freeze-drying assisted method. Ceram Int 24:14660–14666
28. Yang Z, Guo X, Xiang W, Hua W, Zhang J, He F, Wang K, Xiao Y, Zhong B (2017) K-doped layered $LiNi_{0.5}Co_{0.2}Mn_{0.3}O_2$ cathode material: towards the superior rate capability and cycling performance. J Alloys Compd 699:358–365
29. Wang J, Yu Y, Li B, Fu T, Xie D, Cai J, Zhao J (2015) Improving the electrochemical properties of $LiNi_{0.5}Co_{0.2}Mn_{0.3}O_2$ at 4.6 V cutoff potential by surface coating with Li_2TiO_3 for lithium-ion batteries. Phys Chem Chem Phys 17(47):32033–32043
30. Chen Y, Li Y, Li W, Cao G, Tang S, Su Q, Deng S, Guo J (2018) High-voltage electrochemical performance of $LiNi_{0.5}Co_{0.2}Mn_{0.3}O_2$ cathode material via the synergetic modification of the Zr/Ti elements. Electrochim Acta 281:48–59
31. Tao T, Chen C, Qi W, Liang B, Yao Y, Lu SG (2018) Antimony doped tin oxide-coated $LiNi_{0.5}Co_{0.2}Mn_{0.3}O_2$ cathode materials with enhanced electrochemical performance for lithium-ion batteries. J Alloys Compd 765:601–607

32. Chen J, Li L, Wu L, Yao Q, Yang H, Liu Z, Xia L, Chen Z, Duan J, Zhong S (2018) Enhanced cycle stability of $Na_{0.9}Ni_{0.45}Mn_{0.55}O_2$ through tailoring O3/P2 hybrid structures for sodium-ion batteries. J Power Sources 406:110–117
33. Xiao W, Wang Z, Zhang Y, Fang R, Yuan Z, Miao C, Yan X, Jiang Y (2018) Enhanced performance of P (VDF-HFP)-based composite polymer electrolytes doped with organic-inorganic hybrid particles PMMA-ZrO_2 for lithium ion batteries. J Power Sources 382:128–134
34. Tong H, Dong P, Zhang J, Zheng J, Yu W, Wei K, Zhang B, Liu Z, Chu D (2018) Cathode material $LiNi_{0.8}Co_{0.1}Mn_{0.1}O_2/LaPO_4$ with high electrochemical performance for lithium-ion batteries. J Alloys Compd 764:44–50
35. Wu X, Li Y, Zhao S, Zeng F, Peng X, Xiang Y, Ruan Q, Gao F, He T, Wu J (2019) Fabrication of F-doped, C-coated $NiCo_2O_4$ nanocomposites and its electrochemical performances for lithium-ion batteries. Solid State Ionics 334:48–55
36. Shi Y, Zhang M, Qian D, Meng YS (2016) Ultrathin Al_2O_3 coatings for improved cycling performance and thermal stability of $LiNi_{0.5}Co_{0.2}Mn_{0.3}O_2$ cathode material. Electrochim Acta 203: 154–161